Proceedings of the 21st ICSMGE, Vienna, Austria, 14 – 19 June 2026. Pistrol, Adam & Schweiger (eds.)
Published by: ÖGG, Austrian Society for Geomechanics, Salzburg, Austria, ISBN 978-3-9503898-4-5
https://doi.org/10.53243/ICSMGE2026-2066

Analysis of desiccation cracking in compacted soils using computed tomography

David Encalada, **Alberto Ledesma**, Pere C. Prat
Department of Civil and Environmental Engineering, UPC-BarcelonaTech, Spain, alberto.ledesma@upc.edu

Auke Barnhoorn
Department of Geoscience and Engineering, TU Delft, Netherlands

ABSTRACT: Desiccation cracking in soils is a critical issue in geotechnical engineering, particularly in arid and semi-arid environments. Although soil shrinkage and cracking have been extensively studied at the laboratory and field scales, the underlying mechanisms of crack initiation and propagation remain insufficiently understood due to the complex thermo-hydro-mechanical interactions involved. This study uses X-ray computed tomography (CT) as a non-invasive technique to visualize and quantify crack formation and soil deformation in compacted clay specimens subjected to drying and wetting cycles. Compacted specimens were prepared on the dry side, at optimum, and on the wet side of the compaction curve, as well as in slurry form, to explore the influence of soil structure on shrinkage and cracking. Ring-shaped specimens were scanned using microCT, and cylindrical specimens with a rough bottom using macroCT to assess crack morphology, propagation patterns, and soil volume changes. Horizontal and vertical cross-sections were analyzed to identify crack orientation, initiation points, and closure behavior upon wetting. Soil structure emerged as a key factor influencing shrinkage behavior and crack development. Dry side specimens exhibited minimal deformation and low cracking, while wet side and slurry specimens experienced significant volume loss and wide crack openings. Crack closure during wetting was partial, with residual flaws promoting re-opening and the formation of additional cracks in subsequent cycles. CT scans also enabled the calculation of void ratio and construction of Soil Shrinkage Curves (SSCs). Results showed that dry side specimens followed S-shaped SSCs, while wet side and slurry specimens exhibited J-shaped curves. The findings highlight the role of compaction, moisture variation, and initial fabric in desiccation cracking and demonstrate the value of CT in investigating unsaturated soil behavior.

KEYWORDS: Unsaturated soils, desiccation cracking, x-ray CT.

1 INTRODUCTION

Clayey soils are sensitive to moisture variations, undergoing shrinkage during drying and swelling during wetting. These volumetric changes lead to the formation of cracks, which adversely impact geotechnical structures. Specifically, they create discontinuities within the soil mass, reducing mechanical resistance (Trabelsi et al., 2012) and increasing pathways for infiltration (Zhang et al., 2014). Applications affected by desiccation cracking include slope stability, landfill liner integrity, dam embankments, pavements, and tailing deposits.

Desiccation cracks form due to the stresses generated by moisture loss and boundary constraints. Traditionally, cracking has been studied through soil strength or shrinkage deformation using the Soil Shrinkage Curve (SSC) (Shannon et al., 2015; Cheng et al., 2020). Through last years, image techniques have been more frequently used to quantify soil cracking, surface deformation, and analyze crack morphology, but they offer limited insight into subsurface processes. In contrast, X-ray computed tomography (CT) offers a non-invasive method to observe internal soil deformation and crack formation in 3D. Previous studies have used CT to examine pore structure evolution (Bottinelli et al., 2016), but still few have linked cracking behavior to soil microstructure (Tang et al., 2019; Zaidi et al., 2021).

This study employs CT scanning to investigate desiccation cracking in compacted soils, with specimens prepared on both the wet and dry sides of the compaction curve, resulting in distinct soil fabrics, to evaluate their influence on crack development. In addition, slurry specimens, fiber-reinforced specimens, and samples analyzed using both macro- and micro-CT scanning were included to provide a comprehensive understanding of desiccation cracking.

2 EXPERIMENTAL METHOD

2.1 *Material*

The soil used in this investigation was Agropolis silty clay (Cordero et al., 2021; Encalada et al., 2023; Najdi et al., 2023), a low plasticity clay with a liquid limit (w_L) of 29% and a plastic limit (w_P) of 17%. Its particle size distribution comprises 48.3% sand (≤ 2 mm), 42.1% silt (≤ 63 μm), and 9.6% of clay (≤ 2 μm).

Two types of molds were used in the specimen preparation. For microCT analysis, ring-shaped specimens were prepared using 3D-printed molds with an inner diameter of 25 mm, an outer diameter of 50 mm, and a height of 20 mm (see Figure 1a). These molds were designed to enhance crack formation by constraining the sample as soil shrinks. The soil was initially moistened until a target water content was reached and left sealed for at least 48 hours to ensure uniform moisture distribution. It was then compacted dynamically in two layers to reach the desired density. These specimens were prepared under varying water content and dry density conditions to represent different points on the compaction curve (dry side, near optimum, and wet side). Slurry specimens were also prepared to replicate remolded soil conditions. Fibers were incorporated into slurry specimens and in those compacted on the wet side of the compaction curve, where higher deformability was expected.

Larger cylindrical specimens were cast in a 150 mm diameter transparent Plexiglas tube with a height of 45 mm to perform macroCT scans. The mold base, 3D-printed with 2mm×2mm square corrugations (Figure 2), was designed to apply a fixed bottom boundary condition.

To investigate the effect of internal reinforcement, some specimens were mixed with fibers (0.05% in dry weight). The use of fibers in soil has shown capacity to inhibit crack propagation (Hernández et al., 2025). Fibers act as distributed reinforcement, bridging microcracks and redistributing stress concentrations, thus improving tensile strength, ductility, and resistance to impact. In this study, polyethylene terephthalate (PET) fibers were used as reinforcement. The fibers had an average length of 50 mm and a diameter of 15 μm. The complete testing plan is summarized in Table 1.

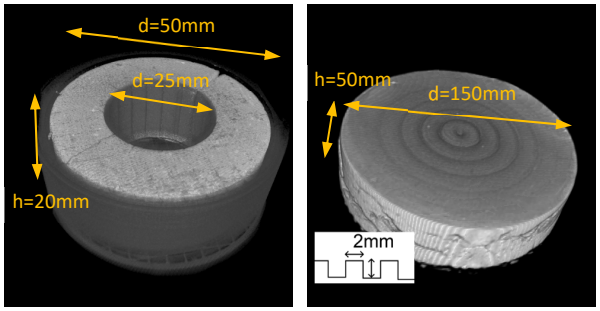

(a) (b)

Figure 1. Specimens (a) Ring shape for microCT, (b) Cylindrical shape with rough base for macroCT.

Table 1. Summary of scanned Agropolis soil specimens under varying initial conditions (w_0, initial gravimetric water content; e_0, initial void ratio).

State		w_0	e_0	%Fiber	Micro-CT	Macro-CT
Dry branch	DB	0.12	0.51	0	2	1
Optimum	O	0.17	0.49	0	2	1
Wet branch	WB	0.21	0.57	0/0.05	3	1
Slurry	S	0.32	0.82	0/0.05	2	-

2.2 *Scanning procedure*

X-ray CT was used for non-destructive, 3D imaging of soil internal structures, allowing for visualization of soil particles, voids, and cracks.

Two scanning systems were employed: (1) MicroCT scans were performed on ring-shaped specimens using a TESCAN CoreTOM system (X-ray source: 30–230 kV, 300 W; detector: 2856×2856 pixels). The voxel size varied between 30.7 and 61.4 µm, depending on the scanning time and resolution requirements. (2) MacroCT scans were conducted on the larger Plexiglas specimens using a Siemens SOMATOM Volume Zoom medical CT scanner (X-ray source: 120 kV, intensity 260 mA). The resolution was kept constant across all macroCT scans.

During scanning, specimens were covered to minimize evaporation. Post-scan weighing confirmed that water loss did not exceed 0.1% of the specimen's initial water content.

2.3 *Image processing*

The CT image analysis was performed using Dragonfly (2022). The workflow included image reconstruction, denoising, and segmentation. A non-local means filter was applied for noise reduction before segmentation (Darbon et al., 2008).

Semantic segmentation was then conducted using a deep learning approach. A U-Net++ architecture (Zhou et al., 2018) was trained with 64-pixel input patches. The architecture was configured with eight initial convolution filters and three depth levels. Training was carried out on a workstation equipped with an NVIDIA Quadro T1000 GPU.

Separate neural networks were trained for each soil texture group to enhance segmentation accuracy and enable more precise classification of solid and void phases. Crack volume quantification was performed through binary morphological operations applied to the segmented images. The X-ray CT additionally allows to assess volume changes by measuring void ratio (e). The void ratio is determined with the following expression:

$$e = \frac{V_V}{V_S} = \frac{V_{CT} - V_S}{V_S} \quad (1)$$

where V_{CT} is soil volume measured by the CT and V_S is the solid volume of soil. For the calculation, the cracks were excluded from the void volume.

3 RESULTS AND DISCUSSION

3.1 *Micro-CT*

Crack propagation in the ring-shaped specimens under various soil fabrics followed similar patterns. Figures 2 and 3 show a mid-height horizontal cross-section of specimens after the first (left image) and second (right image) drying cycles. At the end of each drying cycle, the soil water content reached approximately 2%, a value well below the shrinkage limit (~8%). This low water content corresponds to equilibrium with room relative humidity.

In all specimens, primary cracks consistently propagated radially from the center toward the periphery. These radial cracks were present regardless of compaction condition or the inclusion of fiber reinforcement. For specimens compacted at the dry side (Figure 2a), the radial crack remained narrow (~0.1 mm), yet its reappearance during the second drying cycle—with slight morphological shifts and the formation of a secondary crack—suggests that initial desiccation weakens the soil, promoting further cracking in subsequent cycles.

The specimen compacted at optimum water content (Figure 2b) exhibited a wider initial radial crack (~1 mm) that re-opened during the second cycle, accompanied by minor cracks at the outer tips. This behavior supports the hypothesis that pre-existing cracks act as preferential paths for repeated propagation under cyclic drying.

Specimens compacted on the wet side (Figure 2c) developed a principal crack exceeding 2 mm in width and several minor radial cracks. The second drying cycle re-opened these cracks and initiated circumferential ones, indicating collapse or internal damage during the wetting phase. Such cracks likely originate from weakened zones induced by wetting and suggest structural changes in the soil matrix between cycles.

Fiber-reinforced specimens (Figure 3a and 3c) exhibited limited crack width after the first cycle but showed significant widening during the second. Although fibers restrained crack development in the initial drying, their effectiveness diminished under repeated cycles, with cracks exceeding 1 mm in the fiber-reinforced slurry (Figure 3c). In contrast, the unreinforced slurry (Figure 3b) developed symmetrical radial cracks in the first drying, and additional radial and circumferential cracks emerged in the second. This highlights that slurry specimens were more susceptible to cracking due to their large voids, which act as flaws in the soil matrix.

The conditions for the generation of cracks are a matter of discussion, but there is an increasing consensus that cracks initiate at soil flaws or defects (Shin and Santamarina, 2011), although boundary conditions can also influence cracking as well (Ávila et al., 2011). In fact, the generation of cracks requires a non-uniform strain field, and that can be originated by soil heterogeneities or by constraints due to the boundary conditions. The role of compaction in this process is still poorly understood.

Crack recurrence and new crack formation were consistent across all soil types. The re-opening of initial cracks in the same locations after re-wetting and re-drying supports the concept of residual structural weaknesses in the soil. This behavior was particularly prominent in slurry specimens (Figures 3b and 5b), which showed a significant evolution in crack morphology after the second cycle, including the development of new cracks and larger apertures.

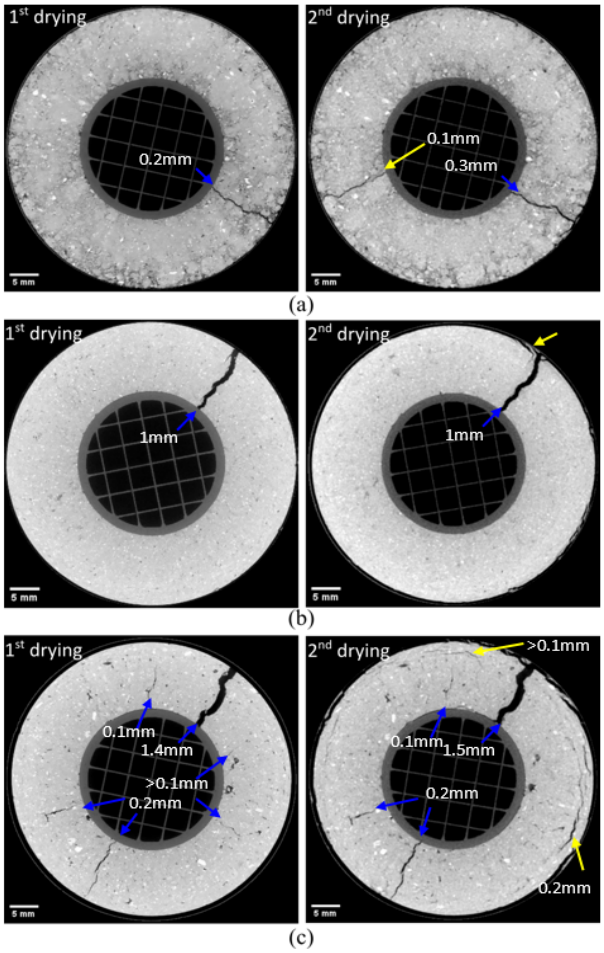

Figure 2. Middle height cross-section after first and second drying cycle for different compacted specimens. (a) Dry side, (b) Optimum, (c) Wet side.

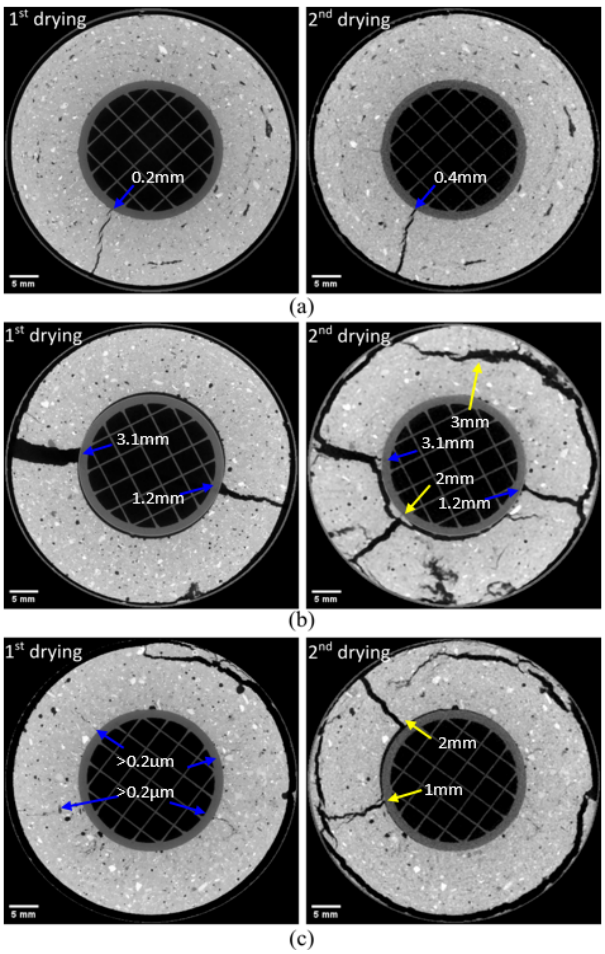

Figure 3. Middle height cross-section after first and second drying cycle for different compacted specimens. (a) Wet side + fibers, (b) Slurry, (c) Slurry + fibers.

For all specimens, the second drying cycle reinforced the existing crack network, confirming that drying–wetting cycles cause irreversible changes to soil structure. While compacted specimens showed more localized changes, slurry and wet side specimens displayed progressive and distributed damage, likely due to soil collapse during wetting and internal flaws (e.g., entrapped air bubbles).

Vertical cross-sections perpendicular to the major primary crack after the first and second drying are shown in Figures 4 and 5. The vertical cross-section revealed predominantly nearly vertical propagation of the primary radial cracks. Cracks generally extended from the surface downward and frequently followed pre-existing flaws. In the dry side specimen (Figure 4a), the radial crack extended from surface to middle height. Upon the second drying, cracks reappeared at the same locations. This suggests that compacted dry side specimens can temporarily heal but retain hidden weaknesses that re-emerge under further desiccation.

In specimens compacted at optimum conditions (Figure 4b), horizontal discontinuities—attributed to the specimen's layered preparation—were evident. After the first drying, vertical cracks intersected these discontinuities, which re-opened during re-wetting and remained partially open.

The wet side specimen (Figure 4c) showed primary cracks extending vertically along its entire length, with numerous adjacent discontinuities. Upon re-saturation, the major crack sealed but with residual openings, and additional discontinuities emerged. These new discontinuities were primarily horizontal and, in a smaller number, parallel to the principal crack.

After the second drying, the principal crack followed its original trace, and new cracks developed, often initiating from the discontinuities created during the preceding wetting process. The wet side specimen with fibers (Figure 5a) exhibited a radial crack that propagated from the surface to its middle height, where it intersected with a horizontal crack. This horizontal crack is likely related to the layered approach used in specimen preparation. Following the second drying cycle, the crack pattern remained consistent with that of the first cycle, though the cracks were slightly wider and more extensive.

Slurry specimens (Figures 5b and 5c) followed a similar trend, showing an increased number of discontinuities after re-wetting. Upon second drying, cracks initiated near flaws formed during wetting, indicating that swelling-induced voids act as crack initiation sites. In fiber-reinforced slurries (Figure 5c), although initial cracking was reduced, the second drying led to crack enlargement and new crack formation, confirming that fiber effectiveness weakens under repeated cycles.

While evaporation naturally drives water from the surface, crack initiation did not always originate at the surface. Figures 6–8 demonstrate the complex role of internal flaws and heterogeneities. Figure 6 shows that cracks initiated around pre-existing voids in wet side specimens. While re-wetting closed some cracks, others remained partially open. This highlights the importance of internal flaws in governing crack reactivation.

Figure 7 illustrates vertical crack initiation in slurry with fibers. Initially, macro voids remained crack-free, but new cracks appeared near the surface after wetting. In the second drying cycle, cracks propagated through voids, suggesting that shrinkage targets previously weakened zones.

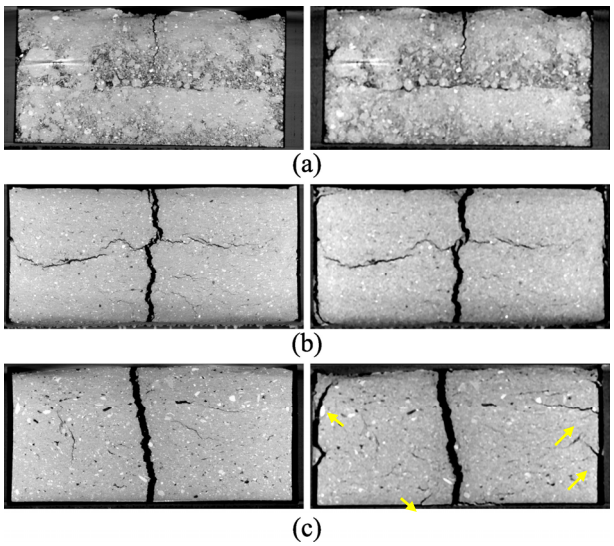

Figure 4. Vertical cross section perpendicular to the major primary crack after first drying (left) and second drying (right). (a) Dry side, (b) Optimum, (d) Wet side.

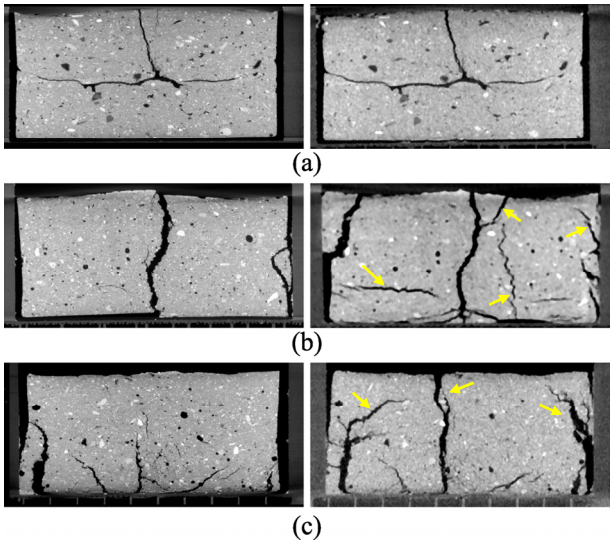

Figure 5. Vertical cross section perpendicular to the major primary crack after first drying (left) and second drying (right). (a) Wet side + fibers, (b) Slurry, (d) Slurry + fibers.

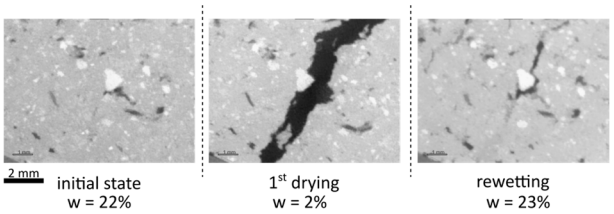

Figure 6. Detailed view of the crack initiation and closure of wet side specimen with different water content (w).

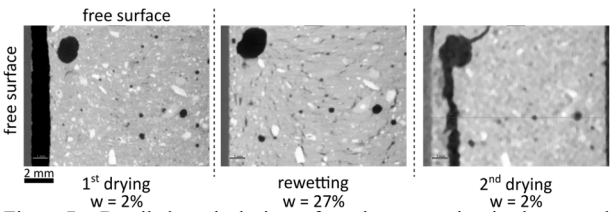

Figure 7. Detailed vertical view of crack propagation in the second drying of slurry specimen with fibers at different water content (w).

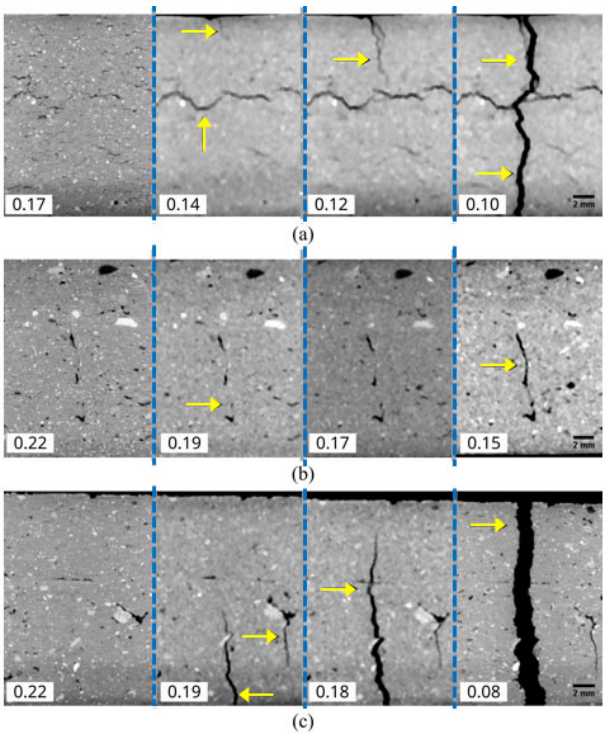

Figure 8. Detailed view of the crack initiation and arrows indicate important flaws and the crack propagation. (a) Optimum water content specimen. (b) Wet side specimen 1. (c) Wet side specimen 2. (Numbers indicate gravimetric water content).

In Figure 8, detailed sequential images confirm that crack initiation can begin from the surface (Figure 8a) or internal flaws (Figures 8b and 8c). In wet side specimen 2 (Figure 8c), the principal crack started at the bottom and grew upward, indicating that the crack initiation location depends on the interaction between structural flaws and drying boundary conditions.

3.2 *Macro-CT*

Figure 9 presents a comparison of the final shrinkage and cracking patterns in three compacted specimens prepared at different initial water contents: dry side (left column), optimum water content (middle column), and wet side (right column). Each set of images includes a vertical cross-section and horizontal cross-sections at the top, middle, and bottom of the specimen, captured after two drying cycles and one wetting stage.

In the dry side specimen, only an angular shrinkage gap developed between the soil and the container wall. No internal cracks were observed. The specimen detached cleanly from the base, and shrinkage occurred uniformly, with the diameter decreasing from 152 mm to 151.6 mm after the first drying, and further to 151.1 mm after the second cycle. The shrinkage gap persisted after wetting, indicating that swelling was restricted, likely due to confinement by the container. These observations reflect the stable aggregate structure typically associated with compaction at low water content.

In contrast, the specimen compacted at optimum water content developed visible cracks. Cracking initiated near the surface and container boundary as the soil began to detach. The most intense cracking occurred below 3.5 cm depth, where vertical cracks propagated inward at angles between 30° and 45°, as measured in top-view projections using Dragonfly 3D visualization software.

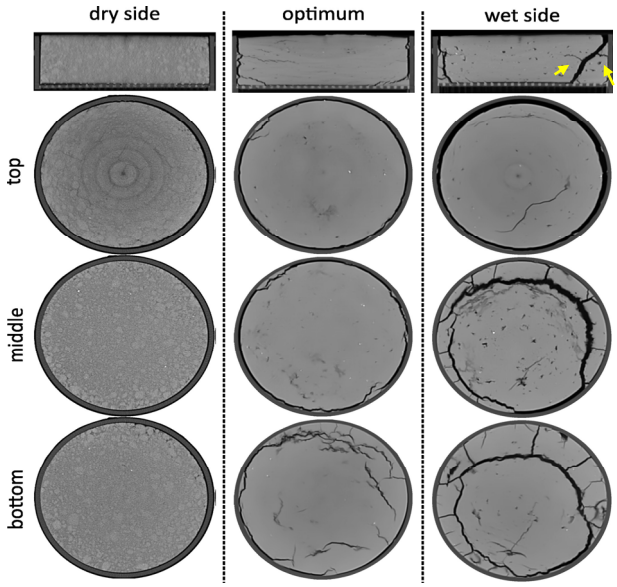

Figure 9. MacroCT results for compacted specimens at dry side, optimum and wet side.

For that specimen compacted at optimum water content, at the final drying stage, the principal cracks reached approximately 0.8 mm in width. Although partial crack closure was observed during wetting, the pattern remained largely unchanged through the second drying cycle, suggesting persistent structural weaknesses.

The wet side specimen exhibited the most pronounced and complex cracking. A shallow surface crack developed early and propagated obliquely downward with further drying. Cracks formed at various angles (up to 60°) and extended through the specimen as detachment progressed from both the sidewall and the bottom. Minor cracks persisted even at a water content of 0.10, and re-wetting induced a temporary surface crack due to reduced strength. This crack remained visible in the second drying cycle, and the overall crack network evolved, with new cracks forming and the principal crack extending in length from 6 cm to 9 cm. The maximum width reached 4 mm, indicating substantial desiccation damage.

These results highlight how soil fabric, governed by compaction water content, strongly influences cracking behavior. Dry side compaction produces a more stable, shrinkage-dominated response with minimal internal cracking. In contrast, specimens compacted at optimum or wet side conditions exhibit pronounced crack development and propagation due to weaker interparticle bonding and higher initial porosity. The evolution of cracks with depth and orientation demonstrates the key role of soil structure in desiccation-induced deformation.

Apparently, the role of double-structure of the soil compacted in the dry side has less influence on cracking development (Demagistri et al., 2018). For those samples, the high stiffness and strength provided by the higher suction value dominates their low sensitivity to cracking. On the contrary, the low suction values and then low stiffness and strength of wet samples allow for more shrinkage and eventually cracking.

3.3 *Soil shrinkage curves*

X-ray CT allowed the non-destructive estimation of soil volume and, consequently, the calculation of void ratio (e) to construct the Soil Shrinkage Curves (SSC) of Agropolis soil. These curves, which plot void ratio against gravimetric water content, describe the volumetric deformation behavior of unsaturated soils.

Figure 10 presents the SSCs obtained from both microCT and macroCT scans of specimens compacted at different water contents—dry side, optimum water content, wet side, and slurry conditions. Crack volumes were excluded from the void volume estimates to ensure that the SSCs reflect intrinsic soil shrinkage behavior rather than structural discontinuities.

The SSCs showed consistent trends across both CT scanning techniques and specimen sizes. The overall shapes of the curves closely resemble those reported for Agroplis soil using traditional volume measurement methods, including digital image analysis (DIA) and paraffin-coated immersion techniques (Encalada et al., 2023), supporting the reliability of CT-based shrinkage characterization.

Soils compacted at optimum water content, on the wet side, and in slurry form exhibited J-shaped SSCs, indicating three classical shrinkage stages: normal, residual, and zero-shrinkage. In contrast, specimens compacted on the dry side displayed an S-shaped (sigmoidal) curve, reflecting the presence of the structural shrinkage stage at water content above 15%. This early-stage behavior is attributed to the aggregate-based structure formed under dry side compaction.

At low water contents (<8%), all specimens converged to a near-constant void ratio, indicating the shrinkage limit beyond which further drying results in negligible volume change. The SSC exhibited low hysteresis between the drying and wetting paths, similar to previous findings, which reported minor hysteresis in the void ratio between the wetting and drying paths (e.g., Fleureau et al., 2002). With the exception of slurry specimens, differences in void ratio between the first and second drying cycles were considerable; the void ratio increased from 0.38 to 0.44 between the first and second drying cycles, which may result from internal structure reorganization or micro-collapse during wetting.

The presence of fibers had a negligible influence on the SSCs, confirming that their principal role is to restrain crack development rather than alter bulk soil compressibility.

The estimation of crack volume based on CT, and expressed as an equivalent void ratio contribution (e_{crack}), quantifies the portion of cracks that can be represented as voids. Dry side specimens displayed a negligible crack ratio (e_{crack} ≈0.0004), consistent with their low deformability, which results in minimal crack development. By contrast, the slurry specimens exhibited significant crack development, with e_{crack} values reaching 0.03 in the microCT tests. For macroCT specimens, which were larger and thus more susceptible to crack propagation, the wet side specimen reached a crack void ratio of 0.17, while the optimum specimen reached 0.057.

Fiber-reinforced specimens exhibited notably reduced crack volumes. The addition of fibers to wet side and slurry specimens reduced e_{crack} to 0.028 and 0.026, respectively, suggesting effective crack mitigation even in inherently unstable soil structures. These results indicate that crack volume is primarily influenced by soil structure and initial water content, with additional influences from specimen size and the presence of fiber reinforcement.

In summary, CT-based shrinkage analysis reliably captured key features of soil volumetric behavior. The method is particularly useful for distinguishing between intrinsic shrinkage (excluding cracks) and crack-induced deformation. The observed SSC trends confirm that compaction water content critically influences the shrinkage behavior of soils: dry side compaction results in stable, aggregate-dominated structures, while wet side and slurry conditions promote volume loss and crack formation. CT scanning thus offers a robust tool for characterizing the mechanical response of unsaturated soils undergoing hydromechanical cycles.

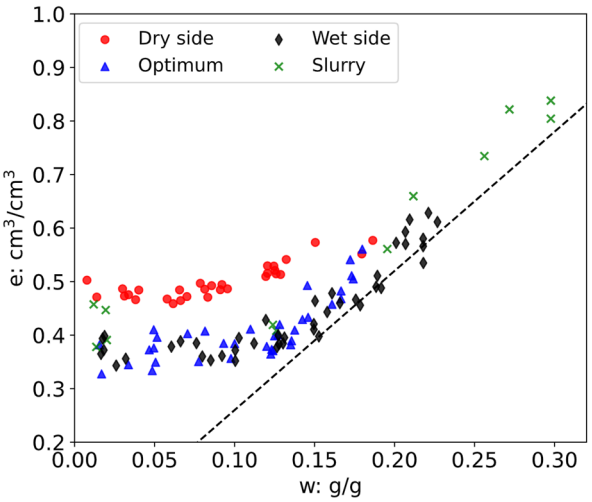

Figure 10. Soil shrinkage curves from CT scans

4 CONCLUSIONS

Volume change due to moisture fluctuations under deformational constraints leads to the development of desiccation cracks in soils. Both, heterogeneities within the soil mass or imposed boundary conditions may generate a non-uniform strain field and eventually cracking. X-ray CT scanning provided a powerful non-destructive tool for tracking soil deformation, visualizing internal structural changes, and observing the initiation, propagation, and re-opening of cracks.

The soil structure, determined by compaction conditions, plays a critical role in controlling shrinkage behavior and crack formation. Specimens compacted at the optimum water content and on the wet side of the compaction curve exhibited greater volume change and were more susceptible to cracking. In contrast, soils compacted on the dry side developed an aggregate-based structure that showed minimal shrinkage and high resistance to crack initiation. This is consistent with the high stiffness and strength associated to the high suction of samples compacted in the dry side.

Wetting and drying cycles are another key factor influencing crack evolution. While wetting promotes partial crack closure through soil swelling, residual flaws often remain along the previous crack paths. These flaws act as preferential zones for crack re-opening during subsequent drying. Additionally, re-wetting can lead to the formation of new discontinuities, which later evolve into visible cracks upon further drying.

Overall, this study demonstrates that both initial soil fabric and hydromechanical cycling govern the deformation and cracking behavior of unsaturated soils. X-ray CT proves to be an effective method for characterizing soil shrinkage and crack development, offering valuable insights for understanding and mitigating desiccation cracking in geotechnical applications.

5 ACKNOWLEDGEMENTS

First author received a grant from AGAUR (Catalan Government) for PhD studies (2019 FI-B 01095). This project has received funding from the European Union's Horizon 2020 research and innovation program under grant agreement No 101005611 for Transnational Access conducted at Delft University of Technology (EPOS-NL Facility Access).

6 REFERENCES

Ávila, G., Ledesma, A., Lloret, A. 2013. One-dimensional cracking model in clayey soils. *Proc. 18th Int. Conf. Soil Mechanics Geotech. Engng.*, Paris, pp. 1077-1080.

Bottinelli, N., Zhou, H., Boivin, P., Zhang, Z.B., Jouquet, P., Hartmann, C. and Peng, X., 2016. Macropores generated during shrinkage in two paddy soils using X-ray micro-computed tomography. *Geoderma*, pp. 78–86.

Cheng, Q., Tang, C.S., guo Chen, Z., El-Maarry, M.R., Zeng, H. and Shi, B., 2020. Tensile behavior of clayey soils during desiccation cracking process. *Engineering Geology*, 279, 105909.

Cordero, J.A., Prat, P.C. and Ledesma, A., 2021. Experimental analysis of desiccation cracks on a clayey silt from a large-scale test in natural conditions. *Engineering Geology*, 292, 106256.

Darbon, J., Cunha, A., Chan, T.F., Osher, S. and Jensen, G.J., 2008. Fast nonlocal filtering applied to electron cryomicroscopy. In: *2008 5th IEEE International Symposium on Biomedical Imaging: From Nano to Macro.* IEEE. pp. 1331–1334.

Demagistri, A., Ledesma, A., Cordero, J., Moreno R., Prat, P.C., Jacinto, A. 2018. Effects of compaction on desiccation cracking of clayey soils. *Proc. 7th Int. Conf. on Unsaturated Soils*, Hong Kong. UNSAT2018.

Dragonfly, 2022. Dragonfly. Available at: https://www.theobjects.com/dragonfly.

Encalada, D., Najdi, A., Mendes, J., Prat, P. and Ledesma, A., 2023. Influence of compaction on the soil shrinkage and swelling curves. *E3S Web of Conferences*, 382, p. 01002.

Fleureau, J.M., Verbrugge, J.C., Huergo, P.J., Gomes Correia, A. and Kheirbek-Saoud, S., 2002. Aspects of the behaviour of compacted clayey soils on drying and wetting paths. *Canadian Geotechnical Journal*, 39(6), pp. 1341–1357.

Hernández, C., Botero, E., Beltrán, G. 2025. The study of fracture mechanics of PET fiber reinforced soils based on flexural tests and imaging techniques. *Transportation Geotechnics*, 51, 101486.

Najdi, A., Encalada, D., Mendes, J., Prat, P.C. and Ledesma, A., 2023. Evaluating innovative direct and indirect soil suction and volumetric measurement techniques for the determination of soil water retention curves following drying and wetting paths. *Engineering Geology*, 322, 107179.

Shannon, B., Kodikara, J. and Rajeev, P., 2015. The use of restrained ring test method for soil desiccation studies. *Geotechnical Testing Journal*, 38(1), pp. 98–112.

Shin, H., Santamarina, J.C. 2011. Desiccation cracks in saturated fine-particle soils: particle-level phenomena and effective-stress analysis. *Geotechnique*, 61(11), pp. 961-972.

Tang, C.S., Zhu, C., Leng, T., Shi, B., Cheng, Q. and Zeng, H., 2019. Three-dimensional characterization of desiccation cracking behavior of compacted clayey soil using X-ray computed tomography. *Engineering Geology*, 255, pp. 1–10.

Trabelsi, H., Jamei, M., Zenzri, H. and Olivella, S., 2012. Crack patterns in clayey soils: Experiments and modeling. *International Journal for Numerical and Analytical Methods in Geomechanics*, 36(11), pp. 1410–1433.

Zaidi, M., Ahfir, N., Alem, A., Taibi, S., El Mansouri, B., Zhang, Y. and Wang, H., 2021. Use of X-ray computed tomography for studying the desiccation cracking and self-healing of fine soil during drying–wetting paths. *Engineering Geology*, 292, 106255.

Zhang, Z.B., Zhou, H., Zhao, Q.G., Lin, H. and Peng, X., 2014. Characteristics of cracks in two paddy soils and their impacts on preferential flow. *Geoderma*, 228–229, pp. 114–121.

Zhou, Z., Siddiquee, M.M.R., Tajbakhsh, N. and Liang, J., 2018. UNet++: A Nested U-Net Architecture for Medical Image Segmentation.